Effect of nonhydrostatic pressure on superconductivity of monatomic iodine: An *ab initio* study

Defang Duan, Xilian Jin, Yanming Ma, Tian Cui,* Bingbing Liu, and Guangtian Zou
State key Laboratory of Superhard Materials, Jilin University, Changchun 130012, People's Republic of China
(Received 28 November 2008; published 17 February 2009)

The dependence of superconducting transition temperature T_c on hydrostatic and nonhydrostatic pressures for monatomic phases of iodine has been studied by first-principles pseudopotential plane-wave method. It is shown that the T_c of both phases II and III under hydrostatic pressures are in agreement with the experimental data while the T_c of phase IV under hydrostatic pressures decreases with increasing pressure, contrary to the experimental results. In order to explore the origin of difference between experimental and theoretical results, we have studied the effect of nonhydrostatic pressure on the superconductivity of monatomic iodine, and found that the symmetry of phase IV changes from face-centered cubic to face-centered orthorhombic (fco) under anisotropic stresses. Further calculations show that the T_c of this fco structure increases with increasing pressure, in good agreement with the experimental results, which is mainly attributed to the nonhydrostatic pressure-induced enhancement of the electronic density of states at the Fermi level and electron-phonon coupling matrix element $\langle I^2 \rangle$.

DOI: 10.1103/PhysRevB.79.064518 PACS number(s): 62.50.−p, 74.62.Fj, 74.25.Kc

I. INTRODUCTION

The superconductivity in many simple elemental solids under high pressure has caused hectic activities over the past two decades. For example, metallic hydrogen has long fascinated high-pressure physicists, which was predicted to be a room-temperature superconductivity,[1] even though its superconductivity is still very hard to realize in laboratory. However, the high-pressure superconductivities in other simple elements have been vastly observed recently, such as sulfur,[2] oxygen,[3] boron,[4] the light element lithium,[5,6] and a surprisingly high T_c of Ca.[7] The superconductivity in the halogen group for iodine and bromine[8–10] have also been successfully discovered with $T_c=1.2$ K and $T_c=1.5$ K at 28 and 90 GPa, respectively. It was reported that the T_c of monatomic iodine decreased with pressure at first but started to increase with pressure for the highest-symmetry phase IV, the face-centered-cubic phase. The mechanism of such a superconductivity with pressure is still unclear. Among various simple elements, iodine can be regarded as a prototype of hydrogen. Therefore, the studies on the superconductivity of iodine under high pressure are also valuable for providing insight into the metallic hydrogen.

Each of solid iodine and bromine forms a diatomic molecular crystal with the base-centered orthorhombic structure (*Cmca* symmetry). Under high pressures, an electronic phase transition from insulator to metal phase occurs at 16 and 60 GPa for solid iodine and bromine without any structural change, respectively.[11–13] An incommensurate phase was observed in iodine at 23 GPa by x-ray diffraction studies,[14] and in bromine at 84 GPa by Raman scattering[15] or 65 GPa by x-ray absorption.[16] Further compression results in a monatomic phase II body-centered orthorhombic structure (bco) (space-group *Immm*) at 30 and 115 GPa for iodine and bromine, respectively.[14,15] For iodine, this body-centered orthorhombic structure was reported to undergo a gradual transition to a body-centered-tetragonal structure (bct) (phase III) with space-group $I4/mmm$ at 43 GPa.[17] A further phase transition to face-centered-cubic structure (fcc) (phase IV) with space-group $Fm\text{-}3m$ occurs at 55 (Ref. 18) or 53 GPa,[19] and this phase persists to at least 276 GPa.[19]

Recently, several theoretical studies[20–23] have been performed to understand the metallization and molecular dissociation in both iodine and bromine solids. As for monatomic phase, the pressure effects on the electron-lattice interaction of fcc iodine have been studied by full-potential linearized augmented plane-wave method (FPLAPW) (Refs. 24 and 25) and full-potential linear muffin-tin orbital method (FPLMTO).[26] However, these calculations showed that the T_c of fcc iodine decreased with increasing pressure, contradicting with the experimental observations.[9] Up to now, the reason for the discrepancy for the pressure dependence of T_c in the fcc phase is not clear.

As we know, if the sample is anisotropically compressed, the crystal lattice can become distorted even if a new phase occurred, such as Fe (Ref. 27) and $NaFeSi_2O_6$ pyroxenes.[28] Molecular-dynamics simulations[29,30] have examined a stable phase subjected to a nonhydrostatic pressure that is not observed under hydrostatic compression. More importantly, the physical properties, in particular superconductivity, is likely to be different for the distorted lattices, such as elements Li (Ref. 6) and Re,[31] organic conductor,[32,33] and high T_c MgB_2.[34] However, little is known about the effect of nonhydrostatic pressure on the superconductivity of solid iodine, which might play a major role in understanding the pressure dependence of T_c observed experimentally. In this paper, we focus our study on the superconductivity of iodine under both hydrostatic and nonhydrostatic pressures by *ab initio* density-functional theory, which has found that the nonhydrostatic pressure effect induces the superconductive behavior of iodine in phase IV that was observed experimentally. In addition, the increase in T_c with pressure is understood in terms of the increase in the electronic density of states (DOS) at the Fermi level and electron-phonon coupling (EPC) matrix element $\langle I^2 \rangle$ caused by nonhydrostatic pressure.

The organization of the paper is as follows: in Sec. II our computational details are described, in Sec. III our results are shown, and in Sec. IV the related discussions are made. Finally, in Sec. V, our results are summarized.

II. METHODOLOGY AND THEORY

A. Computational details

The geometrical optimization, phonon-dispersion, and electron-phonon coupling-constant calculations were carried out using the pseudopotential plane-wave method within the density-functional theory and linear-response theory implemented in the QUANTUM-ESPRESSO package.[35] The generalized gradient approximation (GGA) with the Perdew-Burke-Ernzerhof functional for the exchange correlation was employed.[36] The norm-conserving scheme[37] was used to generate the tight pseudopotential for iodine with electronic configuration of $5s^25p^5$, suitable for the high-pressure study. Convergence tests gave a kinetic-energy cutoff of 60 Ry and Brillouin-zone (BZ) sampling using a grid of spacing $2\pi \times 0.03$ Å^{-1} in all phases. The EPC calculations were performed on a $6\times6\times6$ Monkhorst-Pack (MP) q-point mesh with a denser $24\times24\times24$ k-point mesh in the bco and nonhydrostatic pressure-induced face-centered orthorhombic (fco) phases, and $8\times8\times8$ MP q-point mesh with a denser $32\times32\times32$ k-point mesh in the bct, fcc, and nonhydrostatic pressure-induced body-centered-tetragonal phases for the first BZ integrations. These nonhydrostatic pressure-induced structures will be described in detail in the following text.

B. Calculation of superconducting transition temperature

We evaluated the superconducting transition temperature T_c using the Allen-Dynes[38] modified McMillan equation,[39] which was derived on the basis of the strong-coupling theory,

$$T_c = \frac{\omega_{\log}}{1.2}\exp\left[-\frac{1.04(1+\lambda)}{\lambda-\mu^*(1+0.62\lambda)}\right], \quad (1)$$

$$\lambda = 2\int_0^\infty \frac{\alpha^2F(\omega)}{\omega}d\omega, \quad (2)$$

where λ is the electron-phonon coupling constant, $\omega_{\log}$ is the logarithmic average frequency, and μ^* is the Coulomb pseudopotential. The Eliashberg spectral function $\alpha^2F(\omega)$ is written as

$$\alpha^2F(\omega) = \frac{1}{2\pi N(\varepsilon_F)}\sum_{qv}\frac{\gamma_{qv}}{\omega_{qv}}\delta(\omega-\omega_{qv}), \quad (3)$$

where $N(\varepsilon_F)$ is the electronic DOS at the Fermi level. The linewidth of a phonon mode arising from electron-phonon interaction is given by

$$\gamma_{qv} = 2\pi\omega_{qv}\sum_{kjj'}|g^{qv}_{k+qj',kj}|^2\delta(\varepsilon_{kj}-\varepsilon_F)\delta(\varepsilon_{k+qj'}-\varepsilon_F), \quad (4)$$

where $g^{qv}_{k+qj',kj}$ is the electron-phonon matrix element.

III. RESULTS

Figure 1 summarizes our results concerning the high-pressure behavior of monatomic iodine together with the experimental data. As shown in Fig. 1, the calculated equation

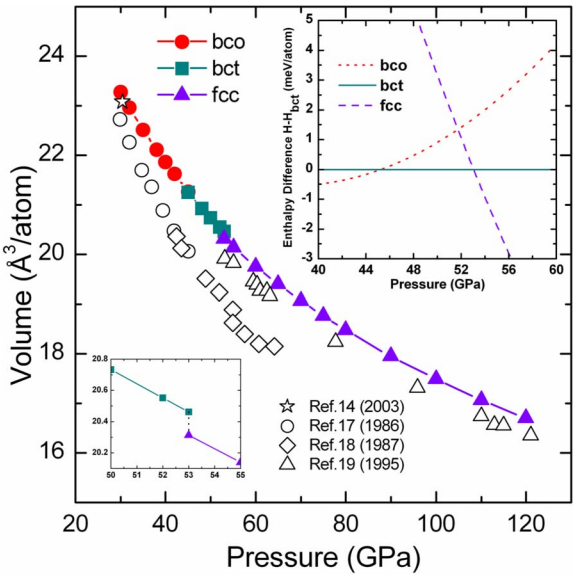

FIG. 1. (Color online) Volume as a function of pressure for three phases of monatomic iodine: bco (red circles), bct (dark cyan squares), and fcc (violet up triangles). The experimental data are denoted by open star (Ref. 14), circles (Ref. 17), diamonds (Ref. 18), and up triangles (Ref. 19). Upper inset: Calculated enthalpy differences (relative to bct structure) as a function of pressure; bco (red dotted line), bct (dark cyan solid line), and fcc (violet dash line). Lower inset: The magnified volume-pressure relation around the bct→fcc phase-transition pressure.

of states (EOS) of monatomic phases is in excellent agreement with the recent experiments. The enthalpy differences (relative to bct structure) as a function of pressure are depicted in the up inset of Fig. 1. We find the following phase-transition sequence with increasing pressure: from bco (phase II) to bct (phase III) at 45 GPa then to fcc (phase IV) at 53 GPa. These compare extremely well with the experimental transition pressures of 43,[17] and 55 or 53 GPa,[18,19] respectively. Moreover, the calculated volume change is continuous for bco to bct transition suggesting a second-order character while the volume collapses with 1% for bct to fcc transition supporting a first-order nature. This again is in accord with experimental observation. In addition, the equilibrium lattice parameter, bulk modulus, and the pressure derivative of fcc phase determined by fitting the total energies as a function of volume to the Murnaghan EOS (Ref. 40) together with other theoretical results and the experimental data are listed in Table I. It is found that the current theoretical lattice constant is in good agreement with experimental data within 2.5%. In conclusion, our calculations are able to reproduce the high-pressure behavior of monatomic iodine in a highly satisfactory manner, which strongly supports the choice of pseudopotential and the GGA used.

In Fig. 2, we compare the calculated pressure dependence of T_c for bco, bct, and fcc phases of monatomic iodine with available experimental results. The Coulomb pseudopotential parameter μ^* used here is a standard choice of 0.1. For the bco phase, the superconducting transition temperature T_c decreases with increasing pressure, which is consistent with the experimental data. Similarly to bco, the T_c of bct phase slack

TABLE I. Calculated equilibrium lattice parameters (a_0), bulk modulus (B_0), and the pressure derivative of bulk modulus (B_0') of fcc iodine. The experimental results (Ref. 19) and previous theoretical calculations (Ref. 24) are also shown for comparison.

Fcc structure	a_0 (Å)	B_0 (GPa)	B_0'
This work	5.12	26.48	5.84
FPLAPW	4.98	38.5	4.25
Expt.	4.99	30.38	6.13

decreases with pressure, which also agrees well with the experimental trend. In the case of fcc phase, however, T_c rapid decreases with increasing pressure, contradicting the experimental observations which show a slight increase as the pressure rises.[9] Moreover, T_c jumps to 2.1 K at the transition point which is nearly twice as large as in the bct phase. In the same figure, the previous theoretical results of fcc phase by FPLAPW and FPLMTO methods[25,26] are included. It can be seen that the pressure dependence of T_c in our present work is consistent with those of the previous theoretical calculation.

To summarize, the T_c of bco and bct phases are in agreement with the experimental results, and the calculated EOS of fcc phase coincides with the experimental data. Nevertheless, it is intriguing that the negative dT_c/dP in the fcc iodine is in contradiction with the experiments. In the following section, we will discuss the effect of nonhydrostatic pressure on superconductivity of fcc iodine.

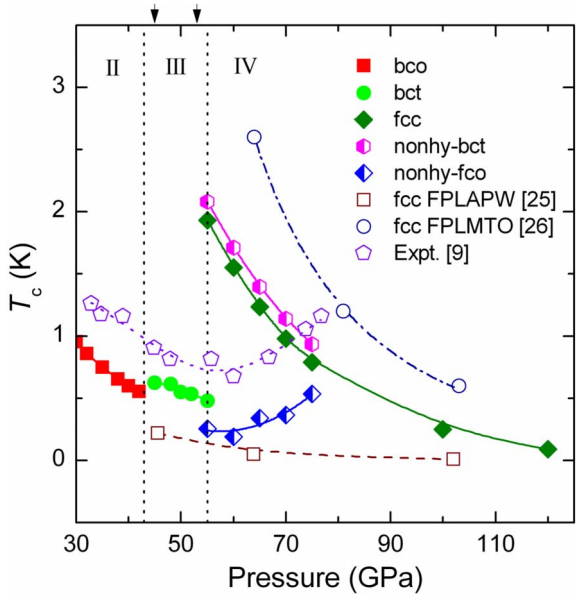

FIG. 2. (Color online) Superconducting transition temperature T_c as a function of pressure. The pressure boundaries between phases II–IV are indicated by dotted lines from experimental results at room temperature and black markers by theoretical results at zero temperature. Results of bco, bct, and fcc phases are denoted by solid red squares, solid green circles, and solid olive diamonds, respectively. Results of nonhydrostatic pressure-induced bct and fco phases are denoted by half-left magenta hexagons and half-left blue diamonds, respectively. The open violet pentagons, wine squares, and royal circles presented experimental data (Ref. 9), FPLAPW (Ref. 25), and FPLMTO (Ref. 26) calculated results, respectively.

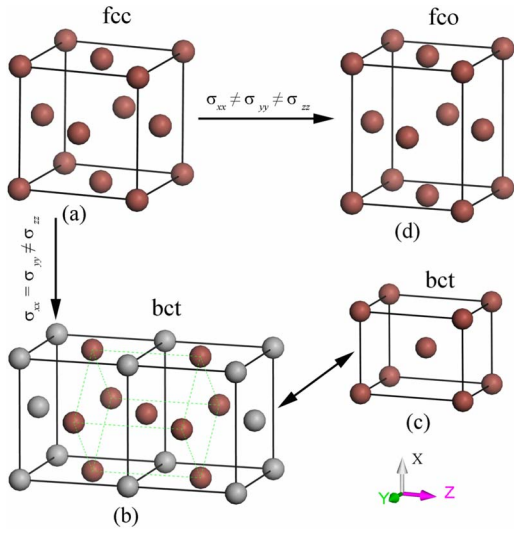

FIG. 3. (Color online) Crystal structures under three kinds of stresses. (a) Crystal structure of fcc under hydrostatic pressure with $\sigma_{xx}=\sigma_{yy}=\sigma_{zz}$, (b) the bct under the uniaxial stresses with $\sigma_{xx}=\sigma_{yy} \neq \sigma_{zz}$, which unit cell is shown by the dotted lines, (c) the redefined unit cell of bct in (b) with $c/a<\sqrt{2}$, and (d) the fco structure under the anisotropic stresses with $\sigma_{xx} \neq \sigma_{yy} \neq \sigma_{zz}$.

The experimental results of the superconducting transition temperature T_c in fcc iodine were obtained without the use of any pressure medium, which easily suffered an anisotropic character of applied pressure.[9] Here we simulate the pressure-induced effects for different nonhydrostatic stress. The simulations are carried out using the full geometrical optimization based on density-functional theory through the CASTEP code.[41] The optimization is not finished until all the stress components are less than 0.005 GPa. The tolerance in the self-consistent field (SCF) calculation is 5×10^{-7} eV/atom. Convergence tests give a $2\pi \times 0.03$ Å^{-1} grid spacing and 560 eV energy cutoff.

In the following, we investigate the effect of two kinds of nonhydrostatic pressures: the effect of the first one is a uniaxial stress, and the second one is that the stress along each crystal axis is different. When the anisotropic stresses are applied, two unique structures are obtained rather than fcc in phase IV. As shown in Fig. 3(b), a bct structure with symmetry $I4/mmm$, which is a subgroup of $Fm\text{-}3m$, is obtained by applying a small (about 10%) compressive component along the fcc [001] axis (a or b axis). It is noteworthy that the uniaxial bct structure with $c/a>\sqrt{2}$ is different from the hydrostatic bct (phase III) with $c/a<\sqrt{2}$. On the other hand, anisotropically compressed fcc structure by applying three different stresses along each crystal axis leads to a fco structure with symmetry $Fmmm$ [Fig. 3(d)]. In the following we denoted these unique structures as nonhydrostatic pressure bct (nonhy-bct) and nonhydrostatic pressure fco (nonhy-fco) structures, respectively. The values of the stress tensor and equivalent hydrostatic pressure for these structures are listed in Table II.

TABLE II. The electronic DOS at the Fermi level $N(\varepsilon_f)$ (in states/Ry/spin/atom), square root of average square of the phonon frequency $\langle\omega^2\rangle^{1/2}$, logarithmic average of vibrational frequencies $\omega_{\log}$, and EPC constant λ computed under hydrostatic and nonhydrostatic pressures in monatomic iodine at selected pressures. σ_{ij} stands for the diagonal values of the stress tensor applied, where σ_p refers to the mean normal stress.

Phase	$(\sigma_{xx},\sigma_{yy},\sigma_{xx})$ (GPa)	σ_p (GPa)	$N(\varepsilon_f)$	$\langle\omega^2\rangle^{1/2}$ (K)	$\omega_{\log}$ (K)	λ
	(30,30,30)	30	3.8556	167.64	140.92	0.4381
	(35,35,35)	35	3.7210	173.09	151.66	0.4121
Bco	(40,40,40)	40	3.6230	178.38	160.62	0.3923
	(45,45,45)	45	3.5455	201.25	168.34	0.3918
	(50,50,50)	50	3.4850	210.75	176.37	0.3806
Bct	(55,55,55)	55	3.4211	217.49	181.40	0.3706
	(55,55,55)	55	3.8726	201.73	153.68	0.5042
	(65,65,65)	65	3.6346	220.33	171.77	0.4432
Fcc	(75,75,75)	75	3.4428	236.62	187.11	0.4002
	(53.2,53.2,58.6)	55	3.9698	196.31	135.30	0.5322
	(62.8,62.8,69.4)	65	3.7672	216.35	164.46	0.4592
nonhy-bct	(72.5,72.5,80.0)	75	3.5163	232.04	179.85	0.4157
	(52.25,55,57.75)	55	3.3011	220.62	182.98	0.3387
	(57.00,60,63.00)	60	3.2139	228.72	189.77	0.3256
	(61.75,65,68.25)	65	3.2791	232.81	187.84	0.3510
	(67.50,70,72.50)	70	3.3199	238.99	191.42	0.3534
nonhy-fco	(72.40,75,77.60)	75	3.4196	238.32	172.86	0.3798

In Fig. 2, we also show the T_c of nonhy-fco and nonhy-bct structures with pressure. For nonhy-bct structure, the T_c rapidly decreases with a slope $dT_c/dP=-0.054$ K/GPa similar to that of the fcc phase within $dT_c/dP=-0.057$ K/GPa. But it is in contradiction with the experimental results. In case of the nonhy-fco structure, however, the dependence of T_c exhibits a quite different behavior. It is important to note that the superconducting transition temperature T_c increases with $dT_c/dP=0.024$ K/GPa, consistent with the experimental results within a rate of 0.029 K/GPa. The results show that the experimental results are reproduced by nonhy-fco structure very well. From this point of view, we conclude that the nonhydrostatic pressure effect can explain the long debate between the experimental and theory results.

IV. DISCUSSIONS

To probe the origin of the pressure dependence on T_c, we calculate the electronic and dynamical properties, and EPC constant λ of the five structures mentioned in this paper. From the Eq. (1) (assuming μ^* is a constant), two parameters: EPC parameter λ and the logarithmic average frequency $\omega_{\log}$, govern T_c. Values of these parameters computed at selected pressures are summarized in Table II. For the bco, bct, fcc, and nonhy-bct structures, $\omega_{\log}$ increase with pressure while λ decreases but the changing rate of λ exceeds that of $\omega_{\log}$. As a result, the value of T_c decreases with pressure mainly due to the decrease in λ. As for nonhy-fco, it is clear that the calculated λ increases with pressure while the $\omega_{\log}$ does not show any clear dependence on pressure. Thus, the increase in T_c with pressure is mainly from the increase in λ as listed in Table II.

The partial EPC constant λ and phonon spectrum of the fcc, nonhy-bct, and nonhy-fco at 55, 65, and 75 GPa are shown in Fig. 4. The absence of imaginary frequency modes indicates that these structures are stable in the pressure range. To compare the difference among the fcc, nonhy-bct, and nonhy-fco, we choose the same high-symmetry lines and points of the Brillouin zone. For the fcc structure, it can be clearly seen that there is a "softening" in the lowest transverse-acoustic (TA1) mode along the Γ-$K[\xi\xi 0]$ direction, leading a significant electron-phonon contribution, in which a high and broad peak of λ is observed near the q point. As pressure increases, soft vibrational modes gradually fade away, resulting in the intensity of the main peak of λ to decrease correspondingly as shown in Fig. 4(a). So, the decrease in λ of fcc phase under hydrostatic pressure mainly derives from the fadeaway of soft vibrational modes induced by increasing pressure. The nonhy-bct structure shows a quite similar behavior to that of the fcc structure presented in Fig. 4(b): the high peak of λ along the Γ-$S[\xi\xi 0]$ direction due to the softening of TA1 mode is also mainly responsible for the EPC constant λ. The decrease in λ with pressure is mainly attributed to the weakening of the "soft" vibrational mode caused by pressure. For the nonhy-fco structure, there is no obvious soft phonon mode observed. But the intensity of the main peaks of λ is clearly seen that an increase and then a decrease with increasing pressure are shown in Fig. 4(c).

In general, the softening of phonon modes is induced by Fermi-surface (FS) nesting. Two-dimensional Fermi-surface

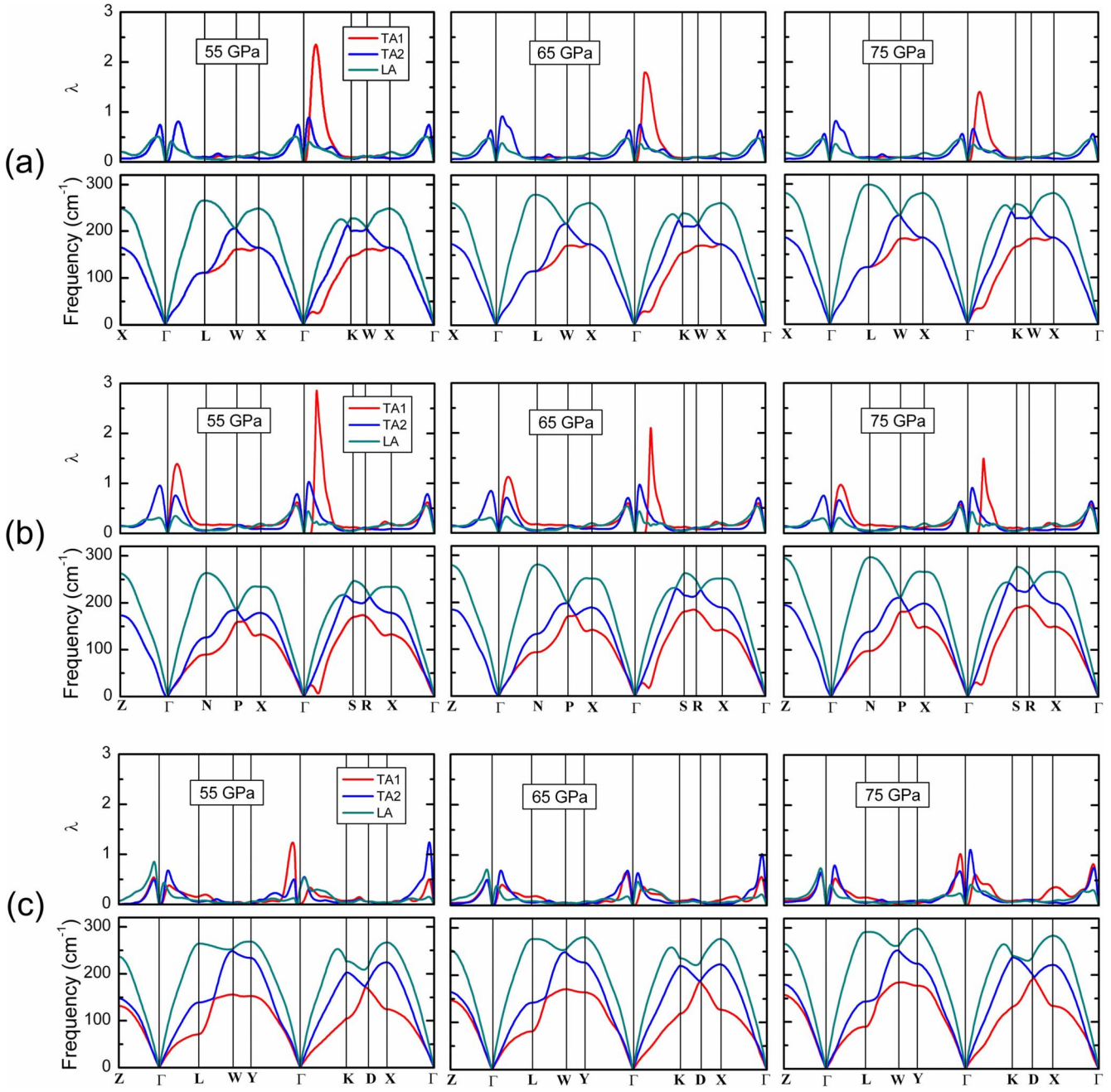

FIG. 4. (Color online) Calculated partial EPC constants λ and phonon spectrum of fcc, nonhy-bct, and nonhy-fco along same high-symmetry lines at selected pressures in (a), (b), and (c), respectively.

cross sections along the (001) plane for the fcc, nonhy-bct, and nonhy-fco structures at 65 GPa are presented in Fig. 5. We clearly recognize nesting vectors (indicated by arrows) connecting fairly flat and parallel lines along the Γ-*K*, Γ-*S*, and Γ-*K* directions for the fcc, nonhy-bct, and nonhy-fco structures, respectively. Note that the nesting of fcc and nonhy-bct is significantly stronger than that of nonhy-fco. The observed phonon softening is a direct consequence of the FS nesting in the fcc and nonhy-bct structures.

In order to obtain more physical insights into the characteristic pressure dependence of EPC constant λ, we evaluate the EPC constant in the following form[39]

$$\lambda = \frac{N(\varepsilon_F)\langle I^2\rangle}{M\langle\omega^2\rangle} = \frac{\eta}{M\langle\omega^2\rangle}, \tag{5}$$

$$\langle I^2\rangle = \frac{\sum_{qv}\sum_{kjj'} |g^{qv}_{k+qj',kj}|^2 \delta(\varepsilon_{kj}-\varepsilon_F)\delta(\varepsilon_{k+qj'}-\varepsilon_F)}{\sum_{qv}\sum_{kjj'} \delta(\varepsilon_{kj}-\varepsilon_F)\delta(\varepsilon_{k+qj'}-\varepsilon_F)}, \tag{6}$$

where η is called Hopfield parameter defined by $\eta = N(\varepsilon_F)\langle I^2\rangle$, and $\langle I^2\rangle$ represents the Fermi-surface average of squared electron-phonon matrix element, which is related to

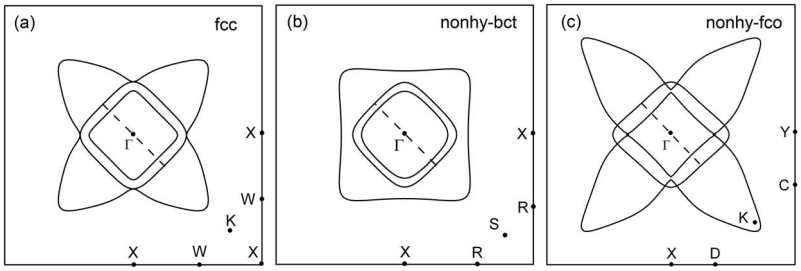

FIG. 5. Two-dimensional Fermi-surface cross sections along the (001) plane for (a) fcc, (b) nonhy-bct, and (c) nonhy-fco structures at 65 GPa. Possible nesting vectors are indicated by dashed line.

the phonon linewidth. M is the mass of the atom and $\langle\omega^2\rangle$ denotes the average of squared phonon frequencies. Note that M is a constant, and that three parameters governing λ are the electronic DOS at the Fermi level $N(\varepsilon_F)$, EPC matrix element $\langle I^2\rangle$, and average of squared phonon frequencies $\langle\omega^2\rangle$. Values of $N(\varepsilon_F)$ and $\langle\omega^2\rangle$ computed at selected pressures are summarized in Table II.

We can judge the EPC matrix $\langle I^2\rangle$ with pressure by the *total* phonon linewidths (defined as the sum of the linewidths at a given q point) which has been used in the theoretical prediction metallic hydrogen.[42] It should be noted that the total phonon linewidth has no clear physical meaning, and $\langle I^2\rangle$ is related to the individual phonon linewidth divided by the corresponding vibration frequencies. The total phonon linewidth along several high-symmetry directions for the fcc, nonhy-bct, and nonhy-fco structures at 55, 65, and 75 GPa are compared in Fig. 6. It is found that the total phonon linewidth does not change very much with pressure for both fcc and nonhy-bct structures, while for the nonhy-fco structure, it rapidly increases with increasing pressure. Another estimate of $\langle I^2\rangle$ is performed as $\langle I^2\rangle_q=(\Sigma_v \gamma_{qv}/\omega_{qv})/C$. The C is a constant with pressure and can be easily calculated. Figure 7 shows the evolution of the $\langle I^2\rangle$ for nonhy-fco structure along several high-symmetry directions with pressure. It is noted that the EPC matrix element $\langle I^2\rangle$ increases under compression, which is also concluded by the phonon linewidth γ_q as shown in Fig. 6(c).

For fcc structure, the value of $N(\varepsilon_F)$ decreases and the value of $\langle\omega^2\rangle$ increases with increasing pressure (see Table II). Since there is no obvious change in $\langle I^2\rangle$ caused by pressure, the decrease in λ is attributed to the combined effect of phonon hardening and the decreased electronic DOS at the Fermi level. The nonhy-bct structure shows similar behavior to the fcc: $N(\varepsilon_f)$ decreases, $\langle\omega^2\rangle$ increases, and $\langle I^2\rangle$ does not change significantly with the increase in pressure.

The second kind of anisotropic compression gives rise to three significant effects. First, the nonhy-fco structure becomes more metallic with increasing pressure as indicated by the increase in $N(\varepsilon_f)$ (see Table II). Second, $\langle I^2\rangle$ increases with pressure shown in Figs. 6(c) and 7. Finally, the $\langle\omega^2\rangle$ increases except for the slight decrease at 75 GPa but the rate of the change is smaller than that of $N(\varepsilon_f)$ and $\langle I^2\rangle$. Therefore, the enhancement of λ is mainly attributed to the combined effect of the increased electronic DOS at the Fermi level and the EPC matrix element $\langle I^2\rangle$.

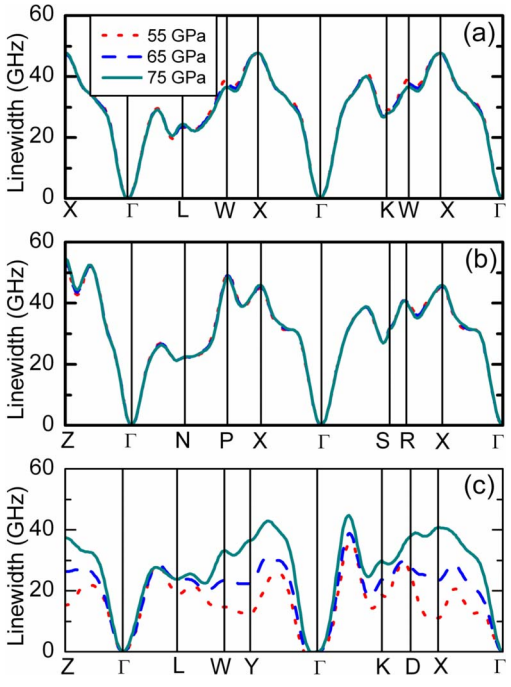

FIG. 6. (Color online) The total phonon linewidths for (a) fcc, (b) nonhy-bct, and (c) nonhy-fco structures at different pressures, shown as red dotted line (55 GPa), blue dash line (65 GPa), and dark cyan solid line (75 GPa) along the high-symmetry directions.

V. CONCLUSIONS

In summary, we have presented a first-principles investigation of the hydrostatic and nonhydrostatic pressure effects on the superconductivity of monatomic iodine. The T_c of both phases II and III are in agreement with the experimental results. In addition, the decreased $N(\varepsilon_F)$ and the phonon hardening are responsible for the decreased T_c in those phases. More importantly, we find that the T_c of nonhydrostatic pressure-induced fco structure increases with increas-

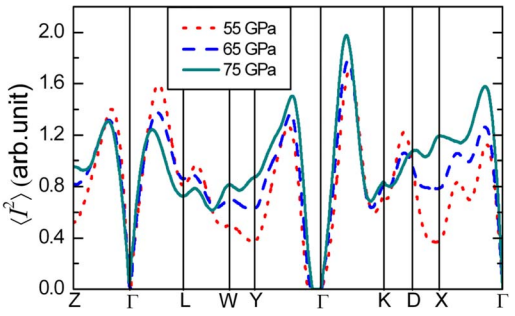

FIG. 7. (Color online) The calculated EPC matrix element $\langle I^2\rangle$ along several high-symmetry directions in the BZ at selected pressures.

ing pressure, consistent with the experimental observations. Our analysis well explains the large conflict between the experimental and theoretical results in phase IV by the nonhydrostatic pressure effect. Further EPC calculations reveal that the observed increase in T_c under pressure in phase IV is mainly attributed to the nonhydrostatic pressure-induced increase in electronic DOS at the Fermi level $N(\varepsilon_F)$ and enhancement of EPC matrix element $\langle I^2 \rangle$. Therefore, the nonhydrostatic pressure effect plays an important role for understanding the superconductivity of monatomic iodine and other materials.

ACKNOWLEDGMENTS

This work was supported by the National Natural Science Foundation of China (Contracts No. 10574053 and No. 10674053), the National Basic Research Program of China (Contracts No. 2005CB724400 and No. 2001CB711201), the Cultivation Fund of the Key Scientific and Technical Innovation Project (Contract No. 2004–295), 2007 Cheung Kong Scholars Programme of China, Changjiang Scholar and Innovative Research Team in University (Contract No. IRT0625), and National Found for Fostering Talents of Basic Science (Contract No. J0730311).

*Author to whom correspondence should be addressed. cuitian@jlu.edu.cn

[1] C. F. Richardson and N. W. Ashcroft, Phys. Rev. Lett. **78**, 118 (1997).
[2] V. V. Struzhkin, R. J. Hemley, H. K. Mao, and Y. A. Timofeev, Nature (London) **390**, 382 (1997).
[3] K. Shimizu, K. Suhara, M. Ikumo, M. I. Eremets, and K. Amaya, Nature (London) **393**, 767 (1998).
[4] M. I. Eremets, V. V. Struzhkin, H. K. Mao, and R. J. Hemley, Science **293**, 272 (2001).
[5] K. Shimizu, H. Ishikawa, D. Takao, T. Yagi, and K. Amaya, Nature (London) **419**, 597 (2002).
[6] S. Deemyad and J. S. Schilling, Phys. Rev. Lett. **91**, 167001 (2003).
[7] T. Yabuuchi, T. Matsuoka, Y. Nakamoto, and K. Shimizu, J. Phys. Soc. Jpn. **75**, 083703 (2006).
[8] K. Shimizu, N. Tamitani, N. Takeshita, M. Ishizuka, K. Amaya, and S. Endo, J. Phys. Soc. Jpn. **61**, 3853 (1992).
[9] K. Shimizu, T. Yamauchi, N. Tamitani, N. Takeshita, M. Ishizuka, K. Amaya, and S. Endo, J. Supercond. **7**, 921 (1994).
[10] K. Shimizu, K. Amaya, and S. Endo, Rev. High Pressure Sci. Technol. **4**, 498 (1995).
[11] B. M. Riggleman and H. G. Drickamer, J. Chem. Phys. **38**, 2721 (1963).
[12] O. Shimomura, K. Takemura, Y. Fujii, S. Minomura, M. Mori, Y. Noda, and Y. Yamada, Phys. Rev. B **18**, 715 (1978).
[13] H. Fujihisa, Y. Fujii, K. Takemura, and O. Shimomura, J. Phys. Chem. Solids **56**, 1439 (1995).
[14] T. Kenichi, S. Kyoko, F. Hiroshi, and O. Mitsuko, Nature (London) **423**, 971 (2003).
[15] T. Kume, T. Hiraoka, Y. Ohya, S. Sasaki, and H. Shimizu, Phys. Rev. Lett. **94**, 065506 (2005).
[16] A. San-Miguel, H. Libotte, M. Gauthier, G. Aquilanti, S. Pascarelli, and J. P. Gaspard, Phys. Rev. Lett. **99**, 015501 (2007).
[17] Y. Fujii, K. Hase, Y. Ohishi, N. Hamaya, and A. Onodera, Solid State Commun. **59**, 85 (1986).
[18] Y. Fujii, K. Hase, N. Hamaya, Y. Ohishi, A. Onodera, O. Shimomura, and K. Takemura, Phys. Rev. Lett. **58**, 796 (1987).
[19] R. Reichlin, A. K. McMahan, M. Ross, S. Martin, J. Hu, R. J. Hemley, H. K. Mao, and Y. Wu, Phys. Rev. B **49**, 3725 (1994).
[20] K. Yamaguchi and H. Miyagi, Phys. Rev. B **57**, 11141 (1998).
[21] M. S. Miao, V. E. Van Doren, and J. L. Martins, Phys. Rev. B **68**, 094106 (2003).
[22] D. Duan, Y. Liu, Y. Ma, Z. Liu, T. Cui, B. Liu, and G. Zou, Phys. Rev. B **76**, 104113 (2007).
[23] Q. Zeng, Z. He, X. San, Y. Ma, F. Tian, T. Cui, B. Liu, G. Zou, and H. K. Mao, Proc. Natl. Acad. Sci. U.S.A. **105**, 4999 (2008).
[24] H. Sakamoto, M. Shirai, and N. Suzuki, J. Phys. Soc. Jpn. **64**, 3860 (1995).
[25] H. Sakamoto, T. Oda, M. Shirai, and N. Suzuki, J. Phys. Soc. Jpn. **65**, 489 (1996).
[26] S. U. Maheswari, H. Nagara, K. Kusakabe, and N. Suzuki, J. Phys. Soc. Jpn. **74**, 3227 (2005).
[27] A. K. Singh, C. Balasingh, H. K. Mao, R. J. Hemley, and J. Shu, J. Appl. Phys. **83**, 7567 (1998).
[28] R. T. Downs and A. K. Singh, J. Phys. Chem. Solids **67**, 1995 (2006).
[29] J. Badro, D. M. Teter, R. T. Downs, P. Gillet, R. J. Hemley, and J.-L. Barrat, Phys. Rev. B **56**, 5797 (1997).
[30] Y. Liang, C. R. Miranda, and S. Scandolo, Phys. Rev. Lett. **99**, 215504 (2007).
[31] C. W. Chu, T. F. Smith, and W. E. Gardner, Phys. Rev. B **1**, 214 (1970).
[32] R. Kondo, S. Kagoshima, and M. Maesato, Phys. Rev. B **67**, 134519 (2003).
[33] K. Murata, S. Kagoshima, S. Yasuzuka, H. Yoshino, and R. Kondo, J. Phys. Soc. Jpn. **75**, 051015 (2006).
[34] S. Deemyad, T. Tomita, J. J. Hamlin, B. R. Beckett, J. S. Schilling, D. G. Hinks, J. D. Jorgensen, S. Lee, and S. Tajima, Physica C **385**, 105 (2003).
[35] A. D. C. S. Baroni, S. de Gironcoli, P. Giannozzi, C. Cavazzoni, G. Ballabio, S. Scandolo, G. Chiarotti, P. Focher, A. Pasquarello, K. Laasonen, A. Trave, R. Car, N. Marzari, and A. Kokalj, http://www.pwscf.org/.
[36] J. P. Perdew, K. Burke, and M. Ernzerhof, Phys. Rev. Lett. **77**, 3865 (1996).
[37] N. Troullier and J. L. Martins, Phys. Rev. B **43**, 1993 (1991).
[38] P. B. Allen and R. C. Dynes, Phys. Rev. B **12**, 905 (1975).
[39] W. L. McMillan, Phys. Rev. **167**, 331 (1968).
[40] F. D. Murnaghan, Proc. Natl. Acad. Sci. U.S.A. **30**, 244 (1944).
[41] M. D. Segall, P. J. D. Lindan, M. J. Probert, C. J. Pickard, P. J. Hasnip, S. J. Clark, and M. C. Payne, J. Phys.: Condens. Matter **14**, 2717 (2002).
[42] L. Zhang, Y. Niu, Q. Li, T. Cui, Y. Wang, Y. Ma, Z. He, and G. Zou, Solid State Commun. **141**, 610 (2007).